



**HAL**  
open science

## Investigation of a rising water surface impacting a motionless cylindrical core in a confined environment within PIV and PVDF gauge measurements

Kilian Croci, V Podeur, M. Arrigoni, Steven Kerampran, M Long, N T Niane

### ► To cite this version:

Kilian Croci, V Podeur, M. Arrigoni, Steven Kerampran, M Long, et al.. Investigation of a rising water surface impacting a motionless cylindrical core in a confined environment within PIV and PVDF gauge measurements. 17ème Journées de l'Hydrodynamique, Nov 2020, Cherbourg-en-Cotentin, France. hal-03023058

**HAL Id: hal-03023058**

**<https://hal.science/hal-03023058v1>**

Submitted on 25 Nov 2020

**HAL** is a multi-disciplinary open access archive for the deposit and dissemination of scientific research documents, whether they are published or not. The documents may come from teaching and research institutions in France or abroad, or from public or private research centers.

L'archive ouverte pluridisciplinaire **HAL**, est destinée au dépôt et à la diffusion de documents scientifiques de niveau recherche, publiés ou non, émanant des établissements d'enseignement et de recherche français ou étrangers, des laboratoires publics ou privés.

**ÉTUDE DE L'IMPACT ENTRE UN NOYAU CYLINDRIQUE FIXE ET UNE SURFACE D'EAU MONTANTE EN MILIEU CONFINÉ AVEC DES MESURES PIV ET DE JAUGE PVDF**

*INVESTIGATION OF A RISING WATER SURFACE IMPACTING A MOTIONLESS CYLINDRICAL CORE IN A CONFINED ENVIRONMENT WITHIN PIV AND PVDF GAUGE MEASUREMENTS*

**K. Croci<sup>(1),\*</sup>, V. Podeur<sup>(1)</sup>, M. Arrigoni<sup>(1)</sup>, S. Kerampran<sup>(1)</sup>, M. Long<sup>(2)</sup>, and N.T. Niane<sup>(2)</sup>**

<sup>(1)</sup>ENSTA Bretagne, IRDL UMR 6027, Brest, France

<sup>(2)</sup>Safran Advanced Turbine Airfoils, a technology platform of Safran Tech, Colombes, France

\*Corresponding author: kilian.croci@gmail.com

**Résumé**

Lors du moulage à la cire perdue de pièces métalliques creuses, les noyaux en céramiques interagissent avec le métal en fusion dans le moule de la pièce. Afin de concevoir un montage expérimental pertinent pour l'étude de cette application industrielle l'interaction fluide/structure peut, dans un premier temps, être étudiée avec un fluide de viscosité similaire (eau) impactant un noyau de géométrie simple (cylindre). Dans cet article, ce type d'interaction fluide/structure en milieu confiné est étudiée expérimentalement avec une surface d'eau, montant verticalement dans une section carrée de  $60 \times 60 \text{ mm}^2$ , qui impacte un cylindre rigide et hydrophile présentant un diamètre de  $40 \text{ mm}$  et une extrémité plate. L'impact est caractérisé par des visualisations d'écoulements par caméra rapide, la mesure de champs de vitesses par Vélocimétrie par Image de Particules (PIV) ainsi que des mesures de pressions dynamiques d'impact (jauge PVDF) qui peuvent être considérés comme une base de données pour la validation de modèles numériques.

**Summary**

During hollow part casting, ceramic cores interact with molten metal injected in the part mould. For convenience this interaction can be, as a first step, investigated using a fluid presenting a similar viscosity (water) impacting a motionless simplified core geometry (cylinder). In the present study, this type of confined fluid/structure interaction is investigated experimentally within a water surface, rising vertically in a  $60 \times 60 \text{ mm}^2$  squared section, impacting a rigid hydrophilic cylinder presenting a  $40 \text{ mm}$  diameter and a flat end. Water entry is characterized within high-speed visualizations, associated velocity flow field measurements with Particle Image Velocimetry (PIV) in addition to impact dynamic pressure measurements (PVDF gauge) which can be considered as experimental database for numerical model validation.

## 1. Introduction

The casting filling process can generate several important defects which can affect the casting quality as mis-run pouring defects which occur when the metal does not completely fill a mould cavity or shrinkage defects with nucleation in the mould due to impurities of dissolved gas inducing holes in final moulded parts [1]. Consequently this filling process represents an important field of interest in steel industry within several studies focusing on the validation of numerical models with experimental data [2, 3, 4, 5] in order to predict and avoid part defects during the casting filling process.

The present experimental investigation takes place in the frame of a *Safran Tech* project dealing with a particular casting filling process, namely the core deflection during hollow blade casting. Hollow blades are usually used in plane or helicopter turbines, facing high operating temperatures, in order to provide an internal cooling effect. During the cast process of such blades [6], the interaction between cores (corresponding to the blade hollow parts) and molten metal in the mould can possibly generate core deflections [7] which can induce part defects or even metal leaks. To enhance the casting process, numerical simulations can be performed with relevant validated models. Even though the numerical approach is not the topic of the present work, a first project step will consist in focusing on the hydrodynamic aspect of the fluid/structure interaction excluding core movements. Based on a similarity in Reynolds number, water can be used instead of molten metal (which presents a similar viscosity) leading to consider classical water entry and fluid/structure interactions [8]. Fluid/structure interaction is classically investigated in the naval industry because of the slamming phenomenon which can induce important structural damages [9] and the studies associated to this field of interest deal mostly with moving bodies impacting a water surface initially considered as steady. The water entry can generate water surface deformations [10, 11], which can be characterized with water velocity flow fields provided by Particle Image Velocimetry (PIV) [12], in addition to important dynamic pressure loads [13, 14] which are mostly due to the impacting body geometry [9]. Finally, depending on several parameters such as the body geometry, its wettability (characterized by the contact angle) or the impact characteristics (impact velocity), the water entry can be considered in two different forms: as hydrophilic with a simple water surface deformation or hydrophobic with the formation of an air-entraining cavity [8, 11].

The purpose of the present paper is to characterize experimentally confined water/core interactions with two main measurement techniques in order to validate numerical models in the case of impacts with motionless cores; the impact pressure on the core will be measured by the use of a PVDF gauge [15] (PolyVynilDiFluoride, a piezoelectric polymer) while Particle Image Velocimetry (PIV) will be performed on image sequences, captured by a high-speed camera, to get water velocity fields during the impact in addition to the water surface profiles, before the impact, which can be deformed depending on the rising velocity due to the interaction between the water flow and the PMMA test section walls. The flow measurement techniques used will be detailed in section 3. These outcomes are considered as an experimental database for numerical model validation and will be analysed regarding the water entry form evolution with the main operating parameter, the Reynolds number.

## 2. Experimental set-up

The experimental set-up has been designed to generate a water surface rising vertically at a constant velocity  $U$  in a square test section before impacting a motionless core. The upstream air supply pressure  $P_s$  is first stabilized with a pressure regulator system and the pressure into the tank (partially filled with water)  $P_t$  is increased linearly. Considering water (density  $\rho = 1000 \text{ kg.m}^{-3}$ ) as an inviscid fluid [5], the tank pressure ramp  $\dot{P}_t$  can be correlated with the rising velocity  $U$ :

$$\dot{P}_t = U \times \rho g \left( 1 + \frac{S}{S_t} \right) \quad (1)$$

with the water surfaces in the tank  $S_t = 57.1 \times 10^3 \text{ mm}^2$  and in the test section  $S = 60 \times 60 = 3.6 \times 10^3 \text{ mm}^2$ .

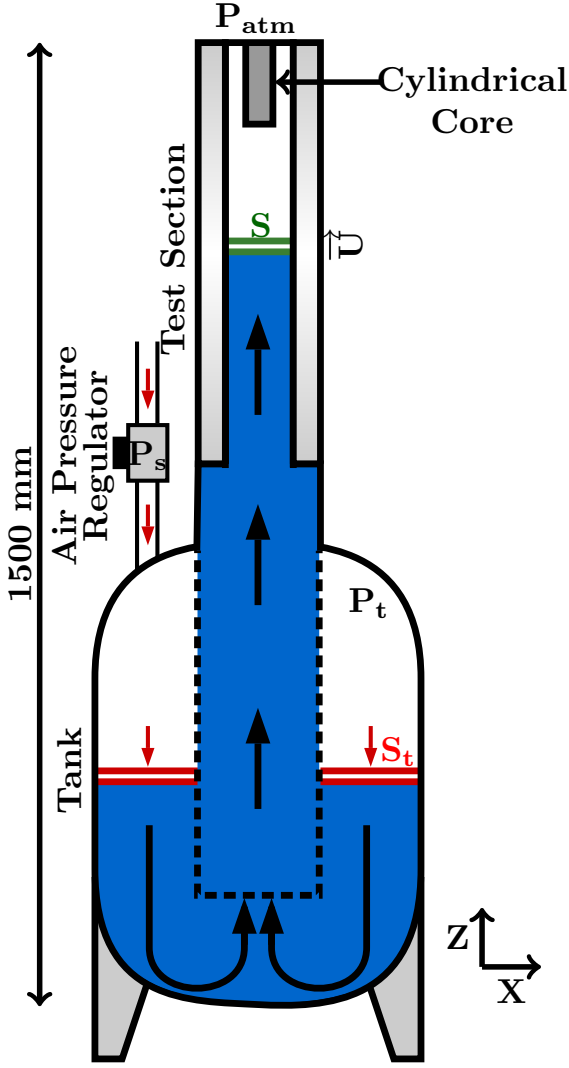


Figure 1. Sketch of the experimental set-up.

The experimental set-up, sketched in Figure 1, is composed of a 40 L capacity tank partially filled with water and connected to a square test-section (with inner surface  $60 \times 60 \text{ mm}^2$ ) made in transparent PMMA to permit flow visualizations with a high-speed camera *PROMON U750* set to  $500 \text{ frames.s}^{-1}$  with a  $800 \times 600 \text{ pixels}^2$  resolution. A round to square contraction nozzle with an area ratio about 5.8 is placed to connect the round vertical tank column to the square test section. The top of the test section is kept open and thus always presents an atmospheric pressure  $P_{atm} = 1.013 \text{ bar}$ . The air pressure into the tank  $P_t$  is recorded at  $50 \text{ Hz}$  with a *Keller PR41X* pressure transmitter (with a  $80 \text{ Pa}$  precision) whereas a stabilized upstream air pressure  $P_s$  is imposed with a pressure servo regulator *Brooks SLA5800* connected to a *IFM PT54* pressure transmitter with 0.5% precision. A compressed air tank, connected to the air supply with a pressure reducing regulator, is placed upstream of the pressure regulation system in order to limit inlet pressure oscillations. The operating temperature  $T$  is measured into the tank with a thermocouple sensor *NTC* and is kept constant at  $20 \pm 1^\circ\text{C}$ .

A cylindrical core, presenting a 40 mm diameter with a length of 100 mm and a flat end surface, is placed at the top of the test section and is impacted by the rising water surface. The  $X, Y, Z$  axis origin point is located at the center of the cylindrical flat end surface (depicted with the red active area in figure 4).

The fixed core (advancing) static contact angle  $\theta$  of the cylindrical core, insulated with aluminium tape as an electromagnetic shield on the PVDF measurements (cf. §3.3), is measured on 50 samples with the static sessile drop technique [16] using the *ImageJ*® plugin “Drop Shape Analysis” with a method based on the Young-Laplace equation [17]. The measurement method accuracy is estimated to  $\pm 2\%$  and the associated statistical standard error is estimated to 1.4% within a 95% confidence limit leading to a measurement uncertainty about 3.4%. The contact angle is then estimated to  $\theta = 74.6^\circ (\pm 3.4\%)$ . Similarly, the contact angle associated to the PMMA test-section is estimated to  $66.4^\circ \pm 3.5\%$ . Considering the similarity within the industrial application previously introduced (§1), the Reynolds number is defined as  $Re = U_w/v$  with the section width  $w = 60 \text{ mm}$  and the water kinematic viscosity  $\nu = 10^{-6} \text{ m}^2.\text{s}^{-1}$ . Another dimensionless number, namely the capillary number  $Ca$ , can characterize the water entry form [8] and is defined as  $Ca = U\rho v/\sigma$  with the water density  $\rho = 1000 \text{ kg.m}^{-3}$  and the surface tension  $\sigma = 7.28 \times 10^{-2} \text{ N.m}^{-1}$ .

### 3. Flow measurement techniques

Flow visualizations and measurements are performed with a *PROMON U750* high-speed camera set to different frame rates and resolutions depending on the application. Image tracking is performed on image sequences to validate equation 1, allowing the use of pressure tank measurements to estimate the rising velocity and the associated Reynolds number. Then PIV and PVDF gauge measurement techniques are introduced, outcome analysis and flow characterization will be investigated in the following sections.

### 3.1 Image tracking technique

**Imaging tracking technique** is first performed to estimate the rising velocity  $U$  on an image sequence and to compare the results with the velocity calculated with equation 1 based on tank pressure measurements.

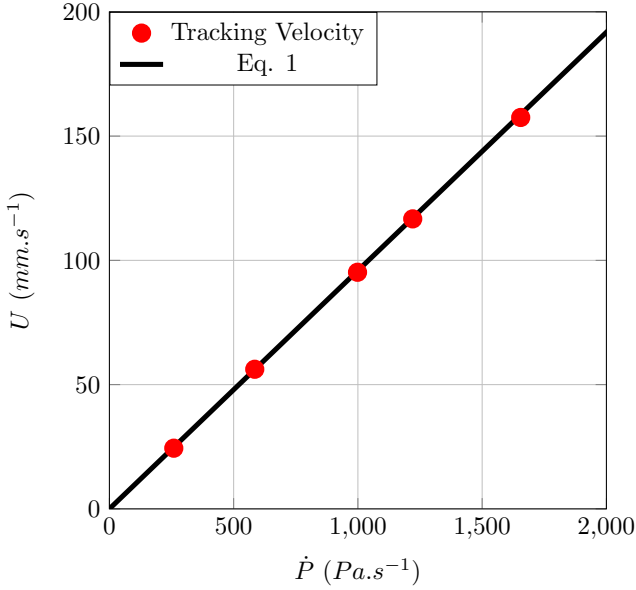


Figure 2. Image tracking velocity measurements comparison with velocity estimation from Equation 1 and pressure ramp measurements.

The sequences are captured at  $500 \text{ frames.s}^{-1}$ , with an exposure time of  $60 \mu s$  with a  $625 \times 714 \text{ pixels}^2$  resolution. The flow is illuminated from behind with a white LED backlight PHLOX. The water surface position is detected after image binarization leading to an estimation of the rising water surface velocity (within  $U \pm 2\%$  precision) along a line positioned at  $X = -25 \text{ mm}$ . The pressure ramp  $\dot{P}_t$  is estimated with the method of least squares with coefficients of determination over 0.999 and a precision estimated to  $\pm 1\%$ . Velocity measurements comparison with associated pressure ramps is presented in Figure 2. Velocity measurements acquired with the image tracking technique appear to be in good agreement with the velocity estimation based on equation 1. Over a pressure ramp of  $\dot{P}_t \simeq 2000 \text{ Pa.s}^{-1}$ , the water surface is disturbed due to the contraction between the column and the test section.

Consequently, pressure tank measurements can be used in the following to estimate relevantly the rising velocity for a range  $0 < \dot{P}_t < 2000 \text{ Pa.s}^{-1} \equiv 0 < U < 192 \text{ mm.s}^{-1} \equiv 0 < Re < 11520$ .

### 3.2 Particle Image Velocimetry (PIV)

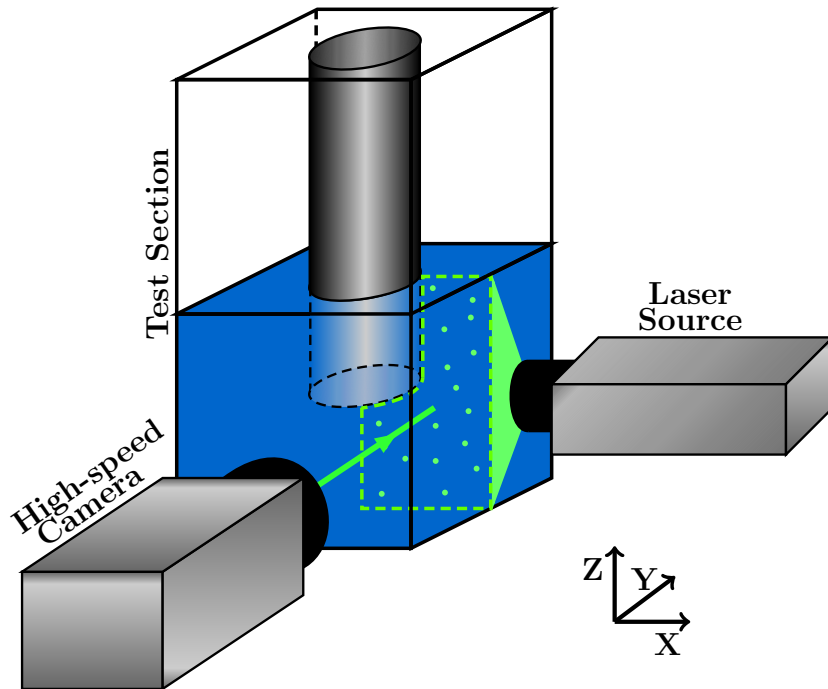


Figure 3. Sketch of the PIV acquisition system. The laser sheet region (green dotted surface) is centered on the middle of the section ( $Y = 0 \text{ mm}$ ) only focusing on the right X-region ( $0 < X < 30 \text{ mm}$ ).

**Particle Image Velocimetry (PIV)** is carried out to estimate velocity fields into the fluid during the water entry [12, 18, 19]. The acquisition system, sketched in Figure 3 is made up of the high-speed camera, set to  $500 \text{ frames.s}^{-1}$  and  $800 \times 600 \text{ pixels}^2$ , and of a  $5 \text{ W}$  power laser source with a wavelength of  $532 \text{ nm}$ . The core width is used as a target reference in order to calibrate the scale in the different images. The velocity fields are finally calculated similarly to Pondeur *et al.* [20] by the open source Matlab toolbox PIVlab [21]. PIV velocities  $u^*$  and  $w^*$  (respectively in  $X$  and  $Z$  direction) are acquired in a region of interest located at  $0 < X < 30 \text{ mm}$  and  $Y = 0 \text{ mm}$ .

### 3.3 Dynamic pressure measurement by the PVDF gauge

**PolyVinylidene Fluoride (PVDF)** pressure gauge, sketched in Figure 4, is stuck on the cylindrical core flat end surface to capture the dynamic pressure peak  $P_{peak}$  during the flow impact. Once the piezoelectric gauge is impacted by the water flow, it produces an electrical signal that can be linearly correlated to the applied pressure (for pressures below  $1000 \text{ bar}$ ) with calibration. The PVDF gauge, which presents a square sensitive area of  $5 \times 5 \text{ mm}^2$ , is implemented on the cylindrical core flat end for calibration. The gauge is calibrated in voltage mode [22] with air flow loading measurements in a shock tube equipped with calibrated *PCB*® sensors [15]. As a result, based on signal correlation applied on three blasts presenting an overpressure about  $0.675 \text{ bar}$ , the PVDF Pressure/Voltage ratio is estimated to  $13.1 \text{ bar.V}^{-1}$  within  $4 \%$  uncertainty. Gauge electrical insulation, in addition to waterproofing, is ensured by non-conductive aluminium tape pasted all over the cylindrical core.

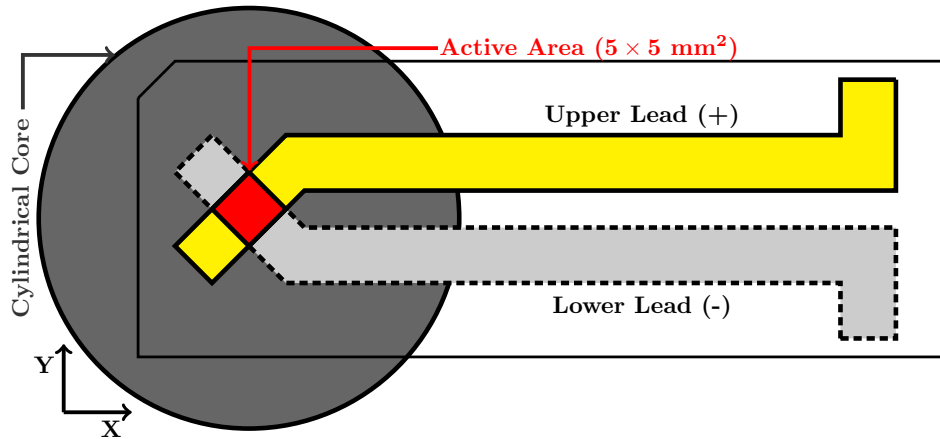


Figure 4. Sketch of the PVDF gauge. The gauge  $25 \text{ mm}^2$  active area (red) is centred on the cylindrical core flat end surface center ( $X = Y = Z = 0 \text{ mm}$ ).

It is important to note that PVDF gauges can capture, in addition to impact pressure peaks, shockwaves induced by cavitation that can occur during high speed water entry [23]. In the present study a low impact velocity is experimented and cavitation is thus beyond our consideration.

All the main study parameters used in §4 to characterise an impact, are presented in Table 1 with their associated uncertainties.

Symbol	Parameters	Range/Value	Unit	Uncertainty
$Re$	Reynolds Number	$6.58 \times 10^3$	—	$\pm 3\%$
$C_a$	Capillary Number	$1.51 \times 10^{-3}$	—	$\pm 3\%$
$P_{peak}$	Over-Pressure Peak	$1.16 \times 10^5$	$Pa$	$\pm 4\%$
$\dot{P}_t$	Pressure Ramp	$1.14 \times 10^3$	$Pa.s^{-1}$	$\pm 1\%$
$U$	Rising Velocity with Eq. 1	110	$mm.s^{-1}$	$\pm 3\%$
$u^*, w^*$	PIV Velocities	$[-50; 242]$	$mm.s^{-1}$	$\pm 5\%$

Tableau 1. Flow parameters, ranges, and estimated uncertainties.

## 4. Experimental flow characterization

In this paper, the characterization of the impact between a rising water surface and a cylindrical core presenting a flat end is provided for a single case presenting flow parameters depicted in Table 1.

### 4.1 Steady curved water surface before impact

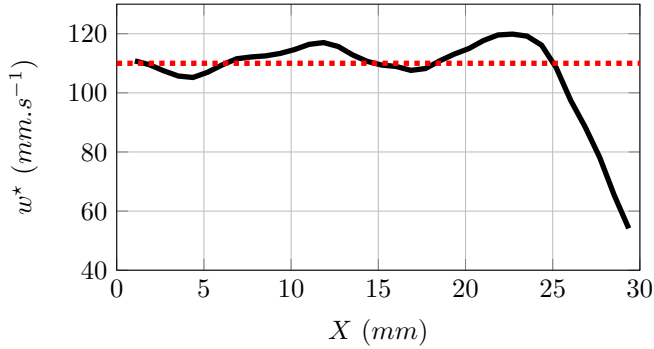


Figure 5. Vertical velocity component  $w^*$  profile before impact averaged on a range  $Z \in [-20; -10]$  mm for  $t \in [-2; -62]$  ms. The red dotted line highlights the associated rising velocity  $U = 110 \text{ mm.s}^{-1}$  estimated with Equation 1.

Contrary to classical studies about water entry in which an object usually impacts an initially flat and steady water surface; in this study the rising water surface can be initially curved, depending on the rising velocity, due to the interaction with test section walls.

The deformation of the water surface due to the confined environment can have an important influence on the water/core impact. The water surface before impact is computed within PIV measurements, averaging the vertical velocity component  $w^*$  before the water entry ( $t \in [-2; -62]$  ms) on a range  $Z \in [-20; -10]$  mm. The velocity profile, presented in figure 5, shows wall-effects on the flow, deforming the water surface, and appears to be consistent with the rising velocity  $U = 110 \text{ mm.s}^{-1}$  estimated with Equation 1.

### 4.2 Water/cylinder interaction

The water impact is characterized by the pressure peak measurement, depicted in figure 6, in addition to the flow velocity profiles just after the impact (figure 7).

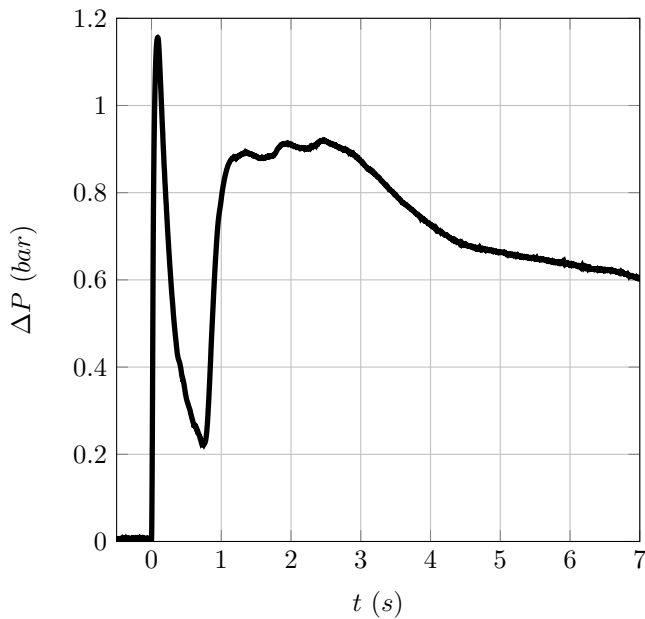
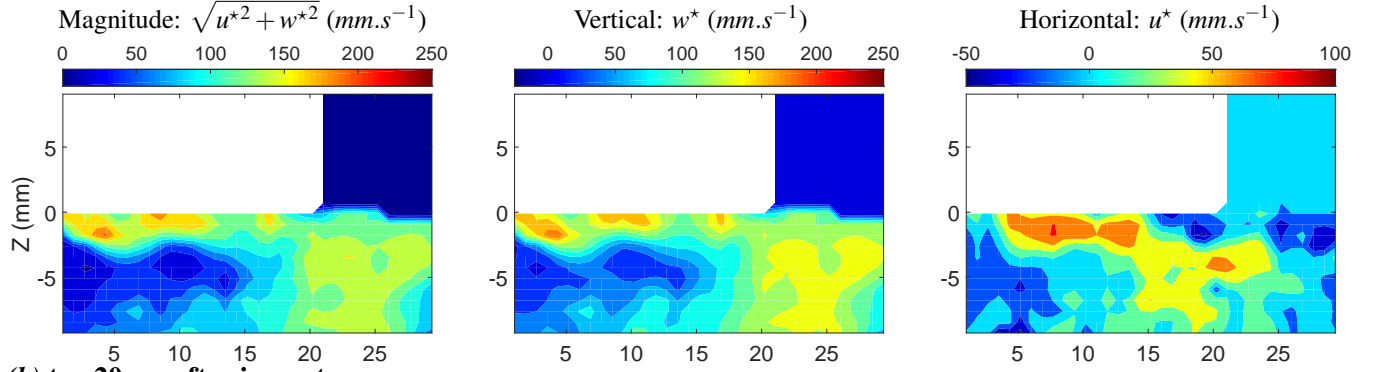


Figure 6. Impact over-pressure  $\Delta P$  evolution with time. The time corresponding to the water/core impact is set to  $t = t_0 = 0$  s. The pressure peak is estimated to  $P_{peak} = 1.16 \text{ bar}$ .

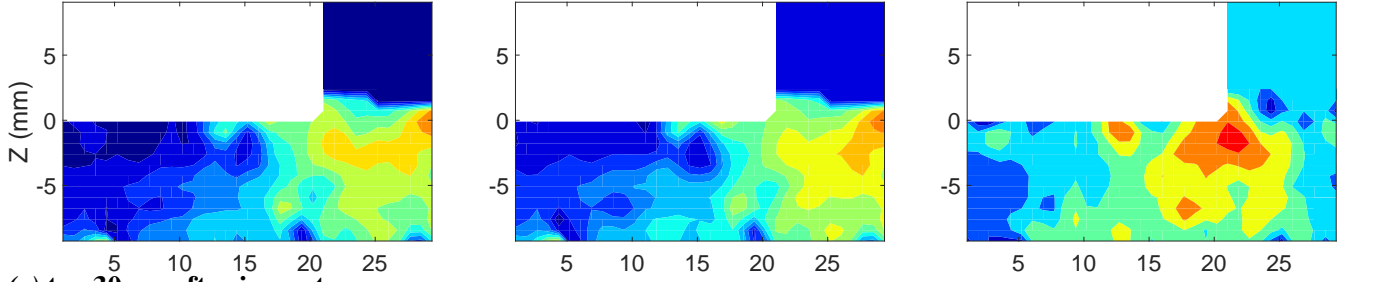
The pressure signal  $\Delta P$  captured by the PVDF gauge (cf. §3.3) is presented in figure 6. The pressure peak, associated to the water entry occurring at  $t = 0$  s, is estimated to  $P_{peak} = 1.16 \text{ bar}$ . The following signal sequence ( $t \in [1; 7]$  s) might correspond to the interaction between water and the pressure gauge connections, due to a default with waterproofing, which can momentarily modify the PVDF calibration.

Classically, the pressure peak can be estimated depending on the sound velocity into water  $c$  as  $P_{peak} = \rho c U \simeq 1.62 \text{ bar}$ . A difference between the measurement and the previous estimation can be due to small variations in core flat end angle but the “air cushioning” phenomenon, which is classically observed in experiments [24], can damp importantly the impact pressure peak within the trap of air pockets during water impact. In the case presented in this paper air cushioning can be detected after impact. In our zone of interest, a bubble with a diameter about 2 mm can be located at  $X = 7.5 \text{ mm}$  and  $Z = 0 \text{ mm}$ .

**(a)  $t = 10$  ms after impact**



**(b)  $t = 20$  ms after impact**



**(c)  $t = 30$  ms after impact**

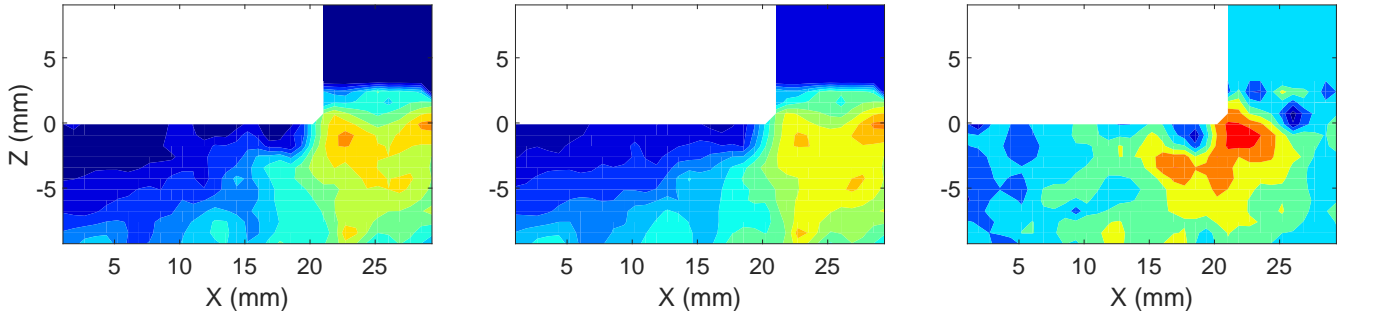


Figure 7. PIV results showing the velocity magnitude and velocity components  $w^*$  and  $u^*$  (left to right) at three different times: (a)  $t = 10$  ms, (b)  $t = 20$  ms and (c)  $t = 30$  ms after impact. The white rectangle corresponds to the location of the cylindrical core. The flow comes from bottom to top.

The velocity flow fields following the impact are presented in figure 7 at the early stages after the impact ( $10 < t < 30$  ms) within vertical and horizontal components and associated velocity magnitude. First, no air-entraining cavities are observable during the impact indicating a hydrophilic nature of the water entry. This result appears to be relevant considering the core contact angle  $\theta = 74.6. < 90^\circ$  and also the small velocity considered with an associated Capillary number  $Ca = 1.51 \times 10^{-3}$ .

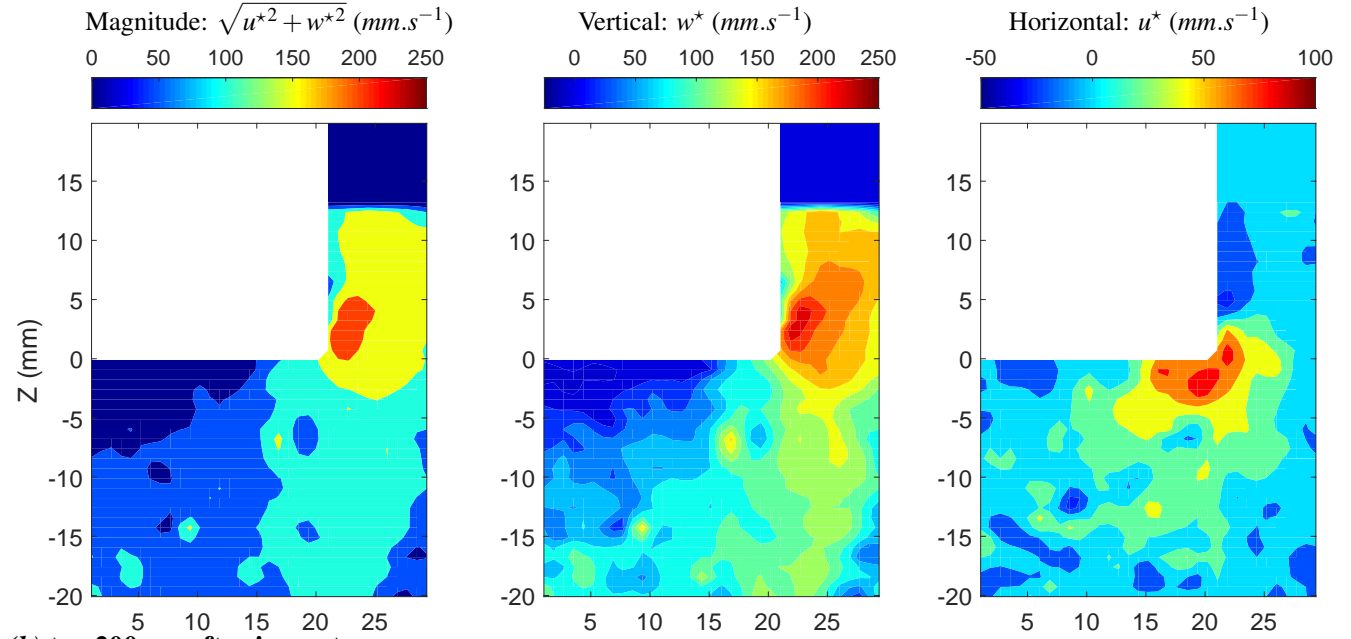
As depicted in figure 7, after the impact loading characterized by the pressure peak, one can see the fluid expansion with important horizontal velocities which are first ( $t = 10$  ms) located under the core flat end surface ( $0 < X < 20$  mm;  $Z = 0$  mm) and, in the next time steps ( $t = 20$  and  $30$  ms), get close to the core corner ( $X = 20$  mm). The fluid is accelerated between the wall and the core side whereas the velocities in the region under the core ( $0 < X < 20$  mm;  $-5 < Z < 0$  mm) decrease quickly.

These results can give an experimental database for the early stages of the impact to compare with diphasic numerical models. However, it would also be interesting to access to established water flow to test the monophasic models.

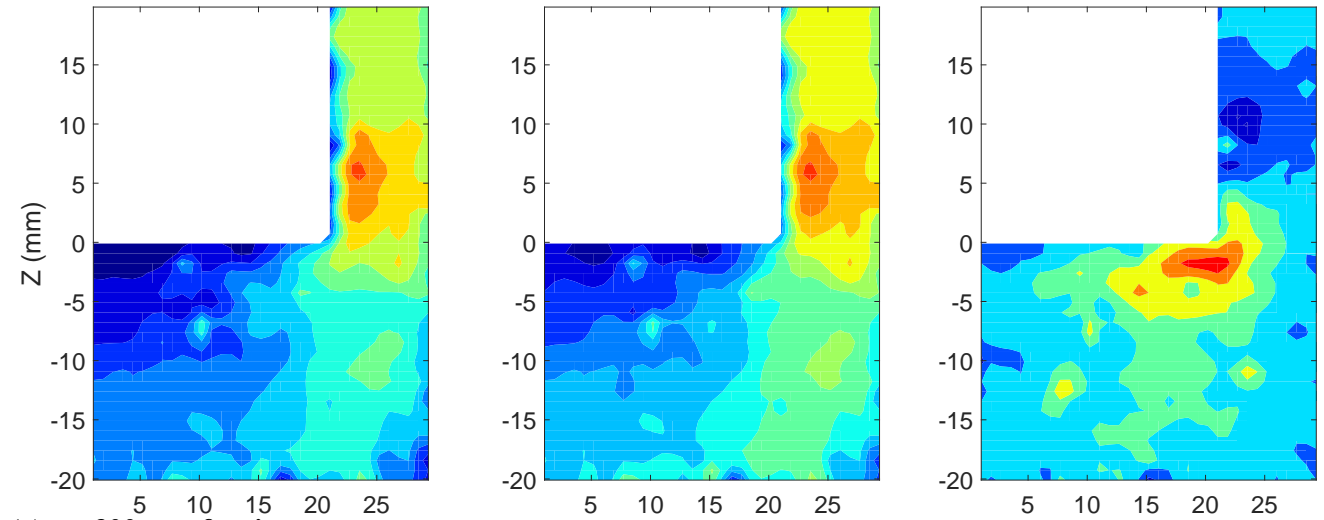
### 4.3 Established flow around the core

The flow establishment around the core is presented in figure 8 for a late time range  $100 < t < 300$  ms.

**(a)  $t = 100$  ms after impact**



**(b)  $t = 200$  ms after impact**



**(c)  $t = 300$  ms after impact**

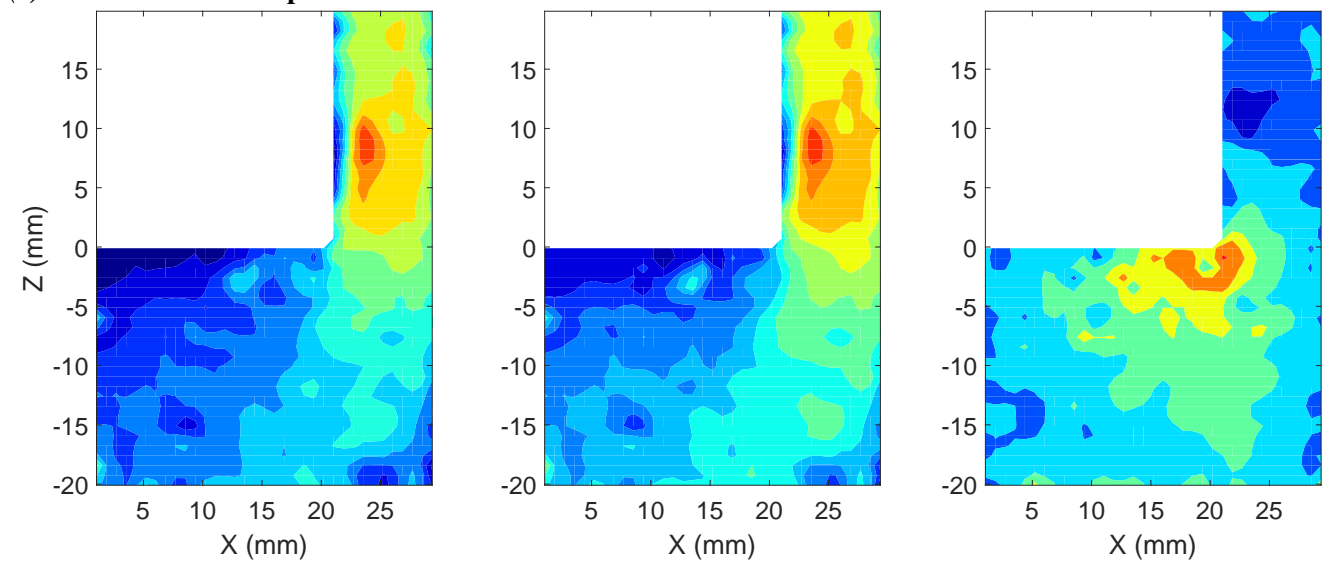


Figure 8. PIV results showing the velocity magnitude and velocity components  $w^*$  and  $u^*$  (left to right) at three different times: (a)  $t = 100$  ms, (b)  $t = 200$  ms and (c)  $t = 300$  ms after impact.

In figure (a), 100 ms after the impact, the water surface is located at  $Z = 13 \text{ mm}$  and alongside the core ( $21 < X < 25 \text{ mm}; 4 < Z < 13 \text{ mm}$ ) a recirculating region characterized by negative horizontal velocities takes place. In the next time steps ( $t = 200$  and  $300 \text{ ms}$ ) the water surface is no longer visible on the velocity fields and the recirculating flow appear to establish near  $Z = 10 \text{ mm}$ .

## 5. Conclusions

In the present study, an experimental set-up designed to study confined water entry has been presented. After estimating characteristic static contact angles with photography, the fluid/structure interaction has been investigated within velocity flow fields (PIV) and impact pressure (with the use of a PVDF gauge) measurements.

As a result, curved water surface before impact has been estimated and the water entry has been characterized with velocity fields around the cylindrical core captured a few moments after the impact ( $t \in [10; 30] \text{ ms}$ ) and, at later times ( $t \in [100; 300] \text{ ms}$ ) within the formation of a recirculating region along the core side. The fluid/structure impact appears to be hydrophilic with an impact pressure peak decreased by the air cushioning phenomenon. The experimental results provided in this study appears to characterize relevantly the confined fluid/structure interactions and can thus be considered as database for numerical model validation.

In future works the core deflection phenomenon, which can occur during hollow part casting process causing important defaults, will be investigated with the experimental set-up presented. The core, which is fixed to the top of the test section in this paper, will then be implemented in the set-up within mechanical slack leading to possible core deflections such as in the hollow blade casting application. Finally, shadowscopy and Schlieren measurements will be performed to access to density gradients during water entry.

## Acknowledgement

The authors would like to acknowledge the financial support granted by *Safran* and their implication in addition to Julien Le Clanche and Frédéric Montel for their assistance in this project.

## References

- [1] G. Bellanger, *Remplissage des pièces moulées en sable. System d'attaque*. Ed. Techniques Ingénieur, 2006.
- [2] Y. Liu, S. Bakhtiyarov, and R. Overfelt, "Numerical modeling and experimental verification of mold filling and evolved gas pressure in lost foam casting process," *Journal of Materials science*, vol. 37, no. 14, pp. 2997–3003, 2002.
- [3] S.-G. Liu, F.-Y. Cao, X.-Y. Zhao, Y.-D. Jia, Z.-L. Ning, and J.-F. Sun, "Characteristics of mold filling and entrainment of oxide film in low pressure casting of a356 alloy," *Materials Science and Engineering: A*, vol. 626, pp. 159 – 164, 2015.
- [4] A. Viswanath, M. Manu, S. Savithri, and U. Pillai, "Numerical simulation and experimental validation of free surface flows during low pressure casting process," *Journal of Materials Processing Technology*, vol. 244, pp. 320 – 330, 2017.
- [5] A. Sanitas, M. Bedel, and M. El Mansori, "Experimental and numerical study of section restriction effects on filling behavior in low-pressure aluminum casting," *Journal of Materials Processing Technology*, vol. 254, pp. 124 – 134, 2018.
- [6] H. Wu, D. Li, and N. Guo, "Fabrication of integral ceramic mold for investment casting of hollow turbine blade based on stereolithography," *Rapid Prototyping Journal*, vol. 15, no. 4, pp. 232–237, 2009.

- [7] D. Wang, J. Sun, A. Dong, G. Zhu, S. Liu, H. Huang, and D. Shu, "Prediction of core deflection in wax injection for investment casting by using svm and bpnn," *The International Journal of Advanced Manufacturing Technology*, vol. 101, no. 5-8, pp. 2165–2173, 2019.
- [8] T. Truscott, B. Epps, and J. Belden, "Water entry of projectiles," *Annual review of fluid mechanics*, vol. 46, pp. 355–378, 2014.
- [9] A. E. M. Alaoui, A. Nême, A. Tassin, and N. Jacques, "Experimental study of coefficients during vertical water entry of axisymmetric rigid shapes at constant speeds," *Applied Ocean Research*, vol. 37, pp. 183–197, 2012.
- [10] J. Aristoff, T. Truscott, A. Techet, and J. Bush, "The water entry of decelerating spheres," *Physics of Fluids*, vol. 22, no. 3, p. 032102, 2010.
- [11] C. Duez, C. Ybert, C. Clanet, and L. Bocquet, "Making a splash with water repellency," *Nature physics*, vol. 3, no. 3, p. 180, 2007.
- [12] M. Jalalisendi, A. Shams, R. Panciroli, and M. Porfiri, "Experimental reconstruction of three-dimensional hydrodynamic loading in water entry problems through particle image velocimetry," *Experiments in Fluids*, vol. 56, no. 2, p. 41, 2015.
- [13] G. De Backer, M. Vantorre, C. Beels, J. De Pré, S. Victor, J. De Rouck, C. Blommaert, and W. Van Paepegem, "Experimental investigation of water impact on axisymmetric bodies," *Applied Ocean Research*, vol. 31, no. 3, pp. 143–156, 2009.
- [14] B. Peseux, L. Gornet, and B. Donguy, "Hydrodynamic impact: numerical and experimental investigations," *Journal of Fluids and Structures*, vol. 21, no. 3, pp. 277–303, 2005.
- [15] M. Arrigoni, F. Bauer, S. Kerampran, J. Le Clanche, and M. Monloubou, "Development of a pvdf pressure gauge for blast loading measurement," *Human Factors and Mechanical Engineering for Defense and Safety*, vol. 2, no. 1, p. 2, 2018.
- [16] C. Duez, *Effets du mouillage en hydrodynamique macroscopique: traînée, impacts et ruissellement*. PhD thesis, 2008.
- [17] A. Stalder, T. Melchior, M. Müller, D. Sage, T. Blu, and M. Unser, "Low-bond axisymmetric drop shape analysis for surface tension and contact angle measurements of sessile drops," *Colloids and Surfaces A: Physicochemical and Engineering Aspects*, vol. 364, no. 1-3, pp. 72–81, 2010.
- [18] R. Panciroli, A. Shams, and M. Porfiri, "Experiments on the water entry of curved wedges: high speed imaging and particle image velocimetry," *Ocean Engineering*, vol. 94, pp. 213–222, 2015.
- [19] A. Shams, M. Jalalisendi, and M. Porfiri, "Experiments on the water entry of asymmetric wedges using particle image velocimetry," *Physics of Fluids*, vol. 27, no. 2, p. 027103, 2015.
- [20] V. Podeur, Y.-M. Scolan, and T. Santagostini, "Experimental and numerical study of a vertical axis turbine for wec application," in *17<sup>ème</sup> Journées de l'Hydrodynamique*, 2020, to appear.
- [21] W. Thielicke and E. Stamhuis, "Pivlab—towards user-friendly, affordable and accurate digital particle image velocimetry in matlab," *Journal of Open Research Software*, vol. 2, no. 1, 2014.
- [22] F. Bauer, "Pvdf shock sensors: applications to polar materials and high explosives," *IEEE Transactions on Ultrasonics, Ferroelectrics, and Frequency Control*, vol. 47, no. 6, pp. 1448–1454, 2000.
- [23] W. Yadong, Y. Xulong, and Z. Yuwen, "Natural cavitation in high speed water entry process," in *Proceedings of the 1st International Conference on Mechanical Engineering and Material Science*, Atlantis Press, 2012.
- [24] H. Mayer and R. Krechetnikov, "Flat plate impact on water," *Journal of Fluid Mechanics*, vol. 850, pp. 1066–1116, 2018.